

Leveraging Global IoT Networks for a Distributed Radio Telescope: Calibration Methods and Performance Analysis

Junming Diao, *Member, IEEE*

Abstract—This paper introduces an innovative approach to radio astronomy by utilizing the global network of Internet of Things (IoT) devices to form a distributed radio telescope. Leveraging existing IoT infrastructure with minimal modifications, the proposed system employs widely dispersed devices to simultaneously capture both astronomical and communication signals. Digital beamforming techniques are applied to align the astronomical signals, effectively minimizing interference from communication sources. Calibration is achieved using multiple distributed satellites transmitting known signals, enabling precise channel estimation and phase correction via GPS localization. We analyze two calibration methods—Phase Alignment Calibration (PAC) and Eigenvalue-Based Calibration (EVC)—and demonstrate that EVC outperforms PAC in environments with significant variation in node performance. Compared to the Green Bank Telescope (GBT), the IoT-based telescope enhances antenna gain by three orders of magnitude and increases survey speed by eight orders of magnitude, owing to the vast number of nodes and expansive field of view (FoV). These findings demonstrate the feasibility and significant advantages of the IoT-enabled telescope, paving the way for cost-effective, high-speed, and widely accessible astronomical observations.

Index Terms—Radio astronomy, Internet of Things (IoT), distributed arrays, beamforming, calibration methods, spectrum sharing, radio astronomy

I. INTRODUCTION

RADIO astronomy is a pivotal tool for exploring the universe, utilizing radio frequencies to study celestial bodies such as stars, galaxies, radio galaxies, quasars, and pulsars. Central to this field are radio telescopes, which typically employ parabolic or spherical reflector antennas to capture faint astronomical signals. These signals are focused onto a feed-receiving system at the reflector’s focal point for analysis.

Maintaining a high signal-to-noise ratio (SNR) amidst faint cosmic radio signals, often ranging from -60 dB to -30 dB, necessitates large reflector antennas and highly sensitive detection systems. As shown in Fig. 1, this requirement has led to the construction of major observatories, such as the 305-meter Arecibo radio telescope, built in 1963 at an inflation-adjusted cost of approximately \$64 million [1], and China’s 500-meter Aperture Spherical Telescope (FAST), completed in 2017 for around \$180 million [2]. These projects reflect a trend toward larger astronomical instruments; however, costs in-

crease exponentially with the size of the reflector antenna [3]–[5].

Furthermore, modern wireless communication networks, which utilize an increasing number of spectrum bands, pose significant challenges to the operations of passive radio telescopes. To protect facilities like the Green Bank Observatory, the United States established the National Radio Quiet Zone (NRQZ) [6]–[8], encompassing 13,000 square miles. However, the proliferation of wireless devices and smart city technologies near NRQZ boundaries in Fig. 1 could lead to increased interference [6], [7], [9], [10]. Additionally, economic development near radio quiet zones is restricted to preserve astronomical observations, limiting local economic opportunities.

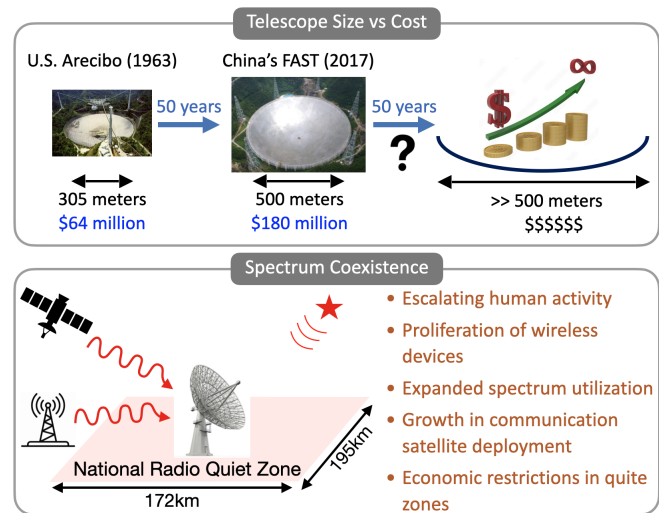


Fig. 1. Challenges faced by current radio telescopes.

This paper introduces an innovative concept that leverages the global deployment of Internet of Things (IoT) devices to develop a groundbreaking radio telescope, utilizing satellites for calibration. The proposed system integrates with existing IoT infrastructure and communication networks with minimal modifications. By sharing the same frequency, time, and location as communication signals, the radio telescope requires no additional hardware or frequency bandwidth. The inspiration for this ambitious project arises from critical technological and economic trends expected to transform communication and astronomical observation, as depicted in Fig. 2.

IoT Expansion: The rapidly increasing number of IoT-

The authors Junming Diao is with the Department of Electrical and Computer Engineering, Mississippi State University, Starkville, MS, USA, E-mail: jdiao@ece.msstate.edu.

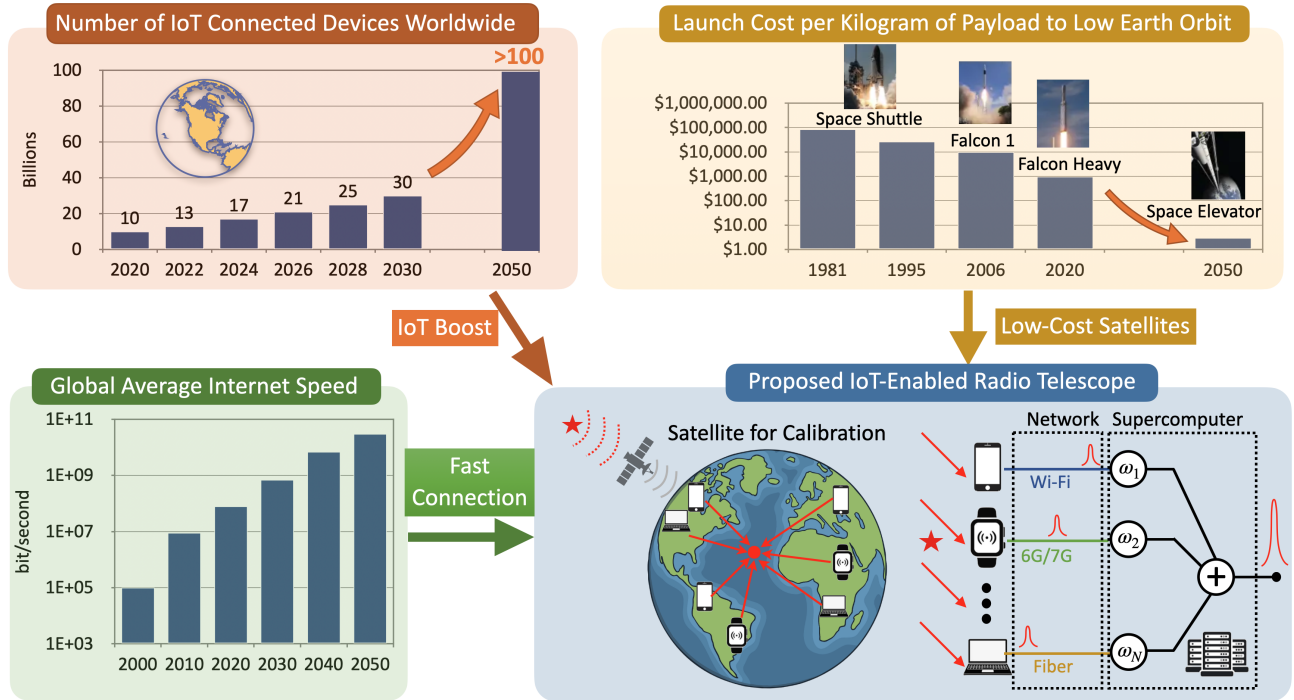


Fig. 2. The proposed IoT-enabled radio telescope concept.

connected devices is fundamental to this proposal. Projections suggest that the global count of IoT devices could exceed 100 billion by 2050 [11]. This vast network of devices, each capable of sending and receiving signals, presents a unique opportunity to create a distributed sensor network acting collectively as a large-scale radio telescope.

Advancements in Connectivity: Propelled by developments in 6G/7G networks and advanced fiber optics, average global internet speeds are expected to surpass 30 Gbps by 2050 [12]. Such enhancements will support the swift transfer of substantial volumes of observational data across this global network to centralized data centers and supercomputing facilities.

Reduced Satellite Costs: The significant reduction in satellite launch costs into low Earth orbit—from the era of the Space Shuttle to future projections involving space elevators by 2050 [13]—has made space-based platforms increasingly accessible. This trend is poised to facilitate the deployment of specialized satellites that not only calibrate but also substantially expand the field of view of the IoT-enabled radio telescope.

Traditional radio telescopes encounter substantial challenges in spectrum sharing primarily due to their structural design and operational environments [14]–[18]. As shown in Fig. 3 (left), these instruments simultaneously capture both astronomical and wireless communication signals at the same frequencies. Due to the physical limitations of using a solid, large single reflector antenna system, they lack the ability to process or differentiate these signals independently [19]–[24]. Consequently, communication signals often disrupt astronomical observations, introducing noise that can obscure or distort valuable scientific data [25]–[31].

The proposed radio telescope design in Fig. 3 (right) ad-

resses these limitations by employing a network of widely dispersed IoT devices. Each device is configured to concurrently capture both astronomical and communication signals at the same frequency, time, and location. These signals are then processed using digital beamforming techniques to phase-align the astronomical signals and maximize the system’s output SNR. Additionally, since the SNR for most astronomical signals is below 0 dB, a threshold near the receiver’s noise floor can be implemented to suppress interference from stronger communication signals. This strategic processing enables the network to focus on and amplify the astronomical signals while effectively minimizing interference from communication signals, which are treated as background noise and subsequently minimized from the final data output.

This capacity for efficient spectrum sharing between astronomical and communication signals opens up groundbreaking opportunities for radio astronomy. It allows for the operation of radio telescopes in more populated or electronically active areas, overcoming a major limitation of traditional telescopes that require secluded, radio-quiet locations. Additionally, it democratizes access to radio astronomy by utilizing the widespread and readily available IoT infrastructure, thereby minimizing the necessity for costly, dedicated radio telescope facilities.

The remainder of this paper is structured as follows. Section II details the system architecture and operational modes of the proposed IoT-enabled radio telescope. Section III explores the calibration methods using single and multiple satellites. In Section IV, we compare Phase Alignment Calibration (PCA) and Eigenvalue-Based Calibration (EBC) approaches. Section V presents a performance estimation and a comparative analysis with the Green Bank Telescope (GBT). Finally, Section

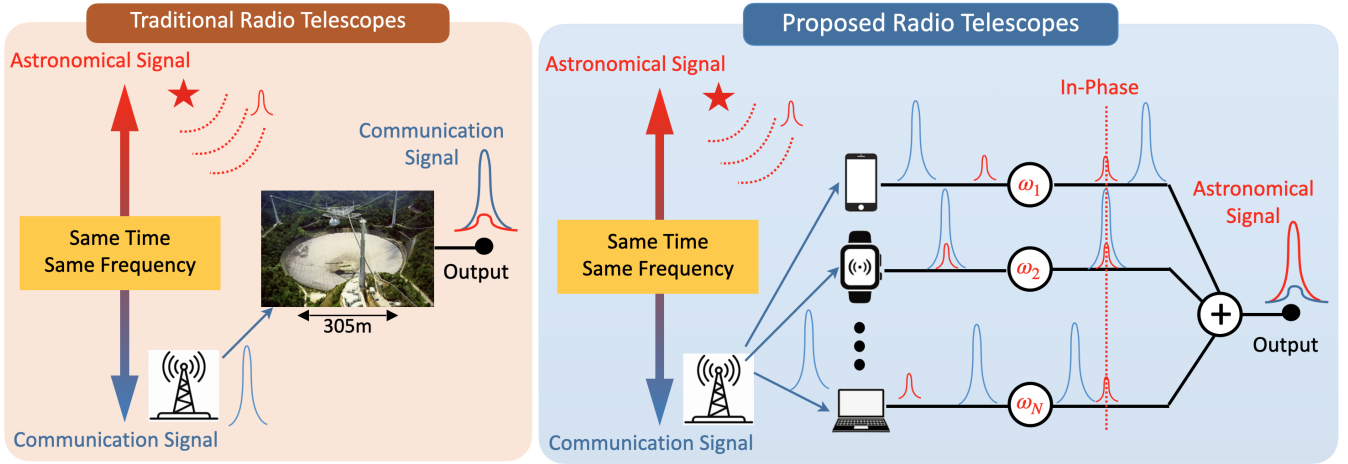


Fig. 3. Enabled spectrum sharing: (left) traditional radio telescope limitations; (right) proposed IoT-enabled telescope facilitating spectrum sharing.

VI concludes the paper.

II. SYSTEM OVERVIEW

In this section, we present an overview of the proposed radio telescope system that leverages the global network of IoT devices. The system is designed for seamless integration with existing IoT infrastructure and communication networks, requiring only minimal modifications.

A. System Architecture

Fig. 4 illustrates the architecture of the proposed system. Each IoT device is equipped with an antenna, low-noise amplifier (LNA), mixer, analog-to-digital converter (ADC), processing unit, and memory. These devices are capable of capturing, digitizing, processing, and temporarily storing timestamped data $\mathbf{x}[i]$.

B. Data Acquisition and Transmission

At each time sample i , the data vector $\mathbf{x}[i]$ collected by the IoT devices is represented as:

$$\mathbf{x}[i] = \mathbf{a} s[i] + \sum_{q=1}^Q \mathbf{v}_q[i] d_q[i] + \mathbf{n}[i], \quad (1)$$

where:

- $s[i]$ is the astronomical signal of interest.
- $d_q[i]$ represents one of Q interfering communication signals.
- $\mathbf{n}[i]$ denotes the noise vector.
- \mathbf{a} and $\mathbf{v}_q[i]$ are normalized array responses to unit amplitude point sources in the far field corresponding to $s[i]$ and $d_q[i]$, respectively.

The data $\mathbf{x}[i]$ can be efficiently transmitted over the communication network to a centralized data center and supercomputing facility. For non-real-time observations, transmission times can be strategically scheduled during periods when devices are typically idle or charging, such as nighttime hours.

C. Signal Processing and Beamforming

The supercomputing facility computes the time-average correlation matrix \mathbf{R} using N samples:

$$\mathbf{R} = \frac{1}{N} \sum_{i=0}^{N-1} \mathbf{x}[i] \mathbf{x}[i]^H, \quad (2)$$

where H denotes the Hermitian transpose. Using this correlation matrix, the beamforming weight vector \mathbf{w} is calculated in the direction of the astronomical signal $s[i]$. The combined output signal is then obtained by:

$$y[i] = \mathbf{w}^H \mathbf{x}[i]. \quad (3)$$

D. Calibration and Observation Modes

As depicted in Fig. 4(b), the proposed system operates in two primary modes: *calibration* and *observation*.

1) *Calibration Mode*: In the calibration mode, specialized satellites act as calibrators by transmitting known calibration signals. These signals are received by the globally distributed IoT devices, enabling precise estimation of channel properties such as time delays and frequency shifts caused by the varied locations and operational environments of the devices. This process ensures synchronization and coherence of the data collected from different devices.

The known calibration signals also aid in characterizing and quantifying noise levels and interference patterns in the received data, enhancing the clarity and accuracy of the subsequent astronomical observations. Calibration facilitates the fine-tuning of each IoT device's parameters, such as gain settings and filter thresholds, thereby maximizing the sensitivity of the receiver system.

The calibration data and timestamps are used to compute the maximum SNR beamforming weight vector $\mathbf{w}_{\max, \text{SNR}}$ by solving the generalized eigenvalue problem:

$$\mathbf{R}_{\text{sat}} \mathbf{w} = \lambda_{\max} \mathbf{R}_n \mathbf{w}, \quad (4)$$

where:

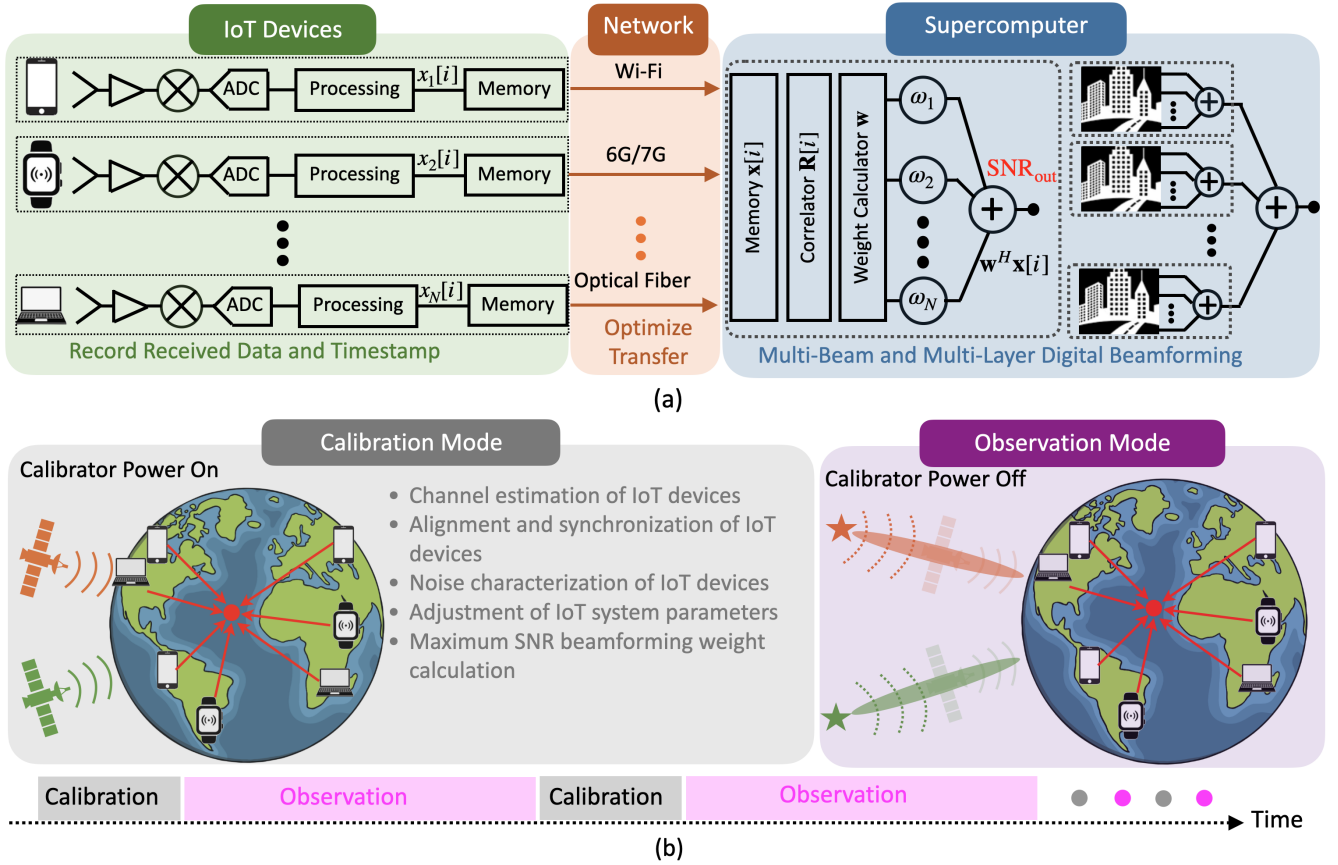


Fig. 4. Overview of the proposed system: (a) system architecture; (b) calibration and observation modes.

- \mathbf{R}_{sat} is the correlation matrix of the received calibration signal from the satellite.
- \mathbf{R}_n is the noise correlation matrix (equal to \mathbf{R}_{off} when the calibration source is off).
- λ_{max} is the maximum eigenvalue.

As shown in Fig. 5, \mathbf{R}_n is obtained during periods when the calibration source is powered off, and \mathbf{R}_{sat} is calculated by subtracting \mathbf{R}_n from the total received correlation matrix when the calibration source is on:

$$\mathbf{R}_{\text{sat}} = \mathbf{R}_{\text{on}} - \mathbf{R}_{\text{off}}. \quad (5)$$

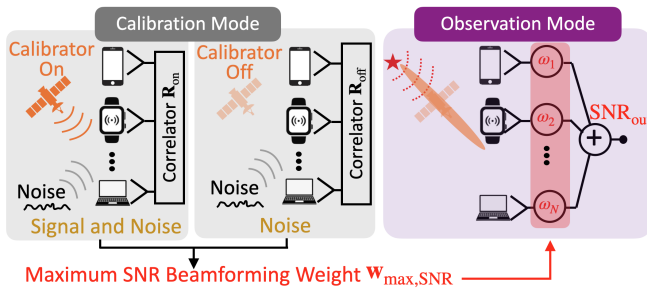


Fig. 5. Signal processing in calibration and observation modes.

2) *Observation Mode*: Once the optimal beamforming weights $\mathbf{w}_{\text{max,SNR}}$ are determined, the system transitions to

observation mode to detect astronomical signals. The output SNR in observation mode is expressed as:

$$\text{SNR}_{\text{out}} = \frac{\mathbf{w}_{\text{max,SNR}}^H \mathbf{R}_{\text{sig}} \mathbf{w}_{\text{max,SNR}}}{\mathbf{w}_{\text{max,SNR}}^H \mathbf{R}_n \mathbf{w}_{\text{max,SNR}}}, \quad (6)$$

where \mathbf{R}_{sig} is the correlation matrix of the astronomical signal.

Due to variations in signal and noise caused by environmental factors, the system periodically alternates between calibration and observation modes to maintain accuracy and coherence in data collection.

E. Multi-Layer Digital Beamforming Strategy

To enhance the efficiency of correlation and beamforming computations, a multi-layer digital beamforming strategy is employed, as illustrated in Fig. 4(a) right. This approach divides the global network of IoT devices into numerous smaller regions where initial beamforming weights are calculated locally. These locally beamformed signals are then aggregated and further processed through a secondary layer of digital beamforming.

This multi-tiered method optimizes computational distribution and improves signal precision by reducing the computational burden on individual nodes and minimizing the required data transmission bandwidth. By processing data hierarchically, the system enhances overall processing efficiency and scalability.

F. Scalability and Multi-Beam Capability

Utilizing multiple satellites for calibration allows the system to perform beam scanning in multiple directions simultaneously. Each satellite can be dedicated to calibrating a specific beam, and by increasing the number of satellites, the system can effectively generate a vast number of beams concurrently. When combined with advanced digital beamforming algorithms, this configuration enables the creation of infinite beams theoretically, significantly enhancing the telescope's flexibility and efficiency.

The ability to calibrate and observe multiple beams concurrently increases the system's capacity for comprehensive sky surveys, facilitating high-resolution imaging and rapid detection of astronomical events. This multi-beam functionality is crucial for monitoring transient phenomena and conducting large-scale mapping of the sky.

G. Interference Suppression and Spectrum Sharing

An essential advantage of the proposed IoT-based radio telescope is its ability to operate alongside existing communication signals in the same frequency bands, times, and locations without requiring additional hardware. Since the SNR for most astronomical signals is below 0 dB, implementing a threshold near the receiver's noise floor suppresses interference from stronger communication signals. This approach effectively filters out signals exceeding the noise threshold, allowing the network to focus on amplifying the weak astronomical signals.

Due to the large spacing between distributed nodes, communication signals at the array output can be treated as background noise. The system minimizes their impact through strategic digital signal processing. By coherently combining weak astronomical signals using digital beamforming, it enhances their detectability despite the presence of stronger interference.

This capability enables efficient spectrum sharing between astronomical observations and communication services. IoT devices can simultaneously perform their primary communication functions while contributing to the radio telescope's data collection, leveraging existing infrastructure and frequency allocations without the need for dedicated hardware or exclusive frequency bands.

H. Non-Technical Consideration: Public Engagement and Incentive Plan

To enhance public engagement and maximize the operational efficiency of the distributed IoT-based radio telescope network, we could have an incentive plan encouraging individuals to contribute their personal devices, such as smartphones and laptops, as active nodes in the array. This transforms everyday devices into valuable assets for astronomical research.

The plan offers compensation to participants through digital credits, service discounts, or payments based on their contribution level, measured by processing power utilized and duration of device engagement. This approach ensures fair compensation while reducing operational costs associated with traditional radio telescopes. By leveraging the ubiquity of

personal devices and existing connectivity, it minimizes the need for extensive physical infrastructure.

Additionally, data transfers can be scheduled during off-peak internet usage hours and lower electricity cost periods, further reducing expenses. Participants can choose their level of involvement to match personal preferences, enabling a broader community to participate as citizen scientists.

Incorporating this incentive plan not only enhances the network's scalability but also fosters public collaboration in scientific discovery. This democratization of astronomical research can increase public interest in science and technology, providing educational opportunities and promoting STEM engagement across diverse populations.

III. NODE PHASE CALIBRATION USING SATELLITES FOR SIMULTANEOUS MULTIPLE BEAMS

In this section, we introduce a calibration method for large-scale distributed node arrays on Earth's surface utilizing multiple calibration satellites, designated as Satellite B. This technique significantly improves array gain and reduces phase errors compared to methods that rely on a single calibration satellite (Satellite A). By deploying multiple satellites for calibration, the system enables simultaneous beam scanning in various directions, theoretically allowing the generation of an infinite number of beams when integrated with digital beamforming algorithms.

A. System Model and Assumptions

We consider a large aperture array consisting of N_{node} nodes randomly distributed along a circular path on Earth's surface. For computational simplicity, we model the array in a two-dimensional plane while accounting for Earth's curvature. The Earth's radius is $R_{\text{earth}} = 6,378$ km.

Each node is assumed to be an isotropic radiator, a common assumption in array antenna theory to simplify analysis [32]. Due to the large separation distances between nodes, mutual coupling effects are neglected.

The array operates at a central frequency of $f = 1.42$ GHz, corresponding to the resonant frequency of neutral hydrogen, which is significant in radio astronomy. The nodes are intended to form a large aperture array with a baseline length L_{baseline} .

The steering angle θ_{steer} ranges from -90° to 90° , allowing for beam scanning across a wide angular range.

Two sets of calibration satellites are employed:

- **Satellite A:** A single calibration satellite positioned at an altitude of h_{satA} above Earth's surface.
- **Satellite B:** Multiple distributed calibration satellites, with a total number of N_{satB} , evenly distributed along an orbital path at an altitude of h_{satB} .

B. Ideal Array Gain

When the beam is steered in the θ_{steer} direction, the active nodes for beamforming described in Fig. 6 are selected within a angle range defined by $\theta_{\text{steer}} \pm \Delta\theta$, where

$$\Delta\theta = \arcsin\left(\frac{L_{\text{baseline}}}{2R_{\text{earth}}}\right). \quad (7)$$

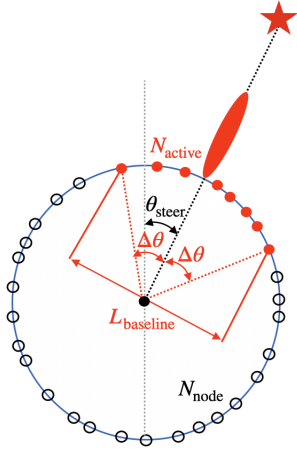


Fig. 6. Schematic of active array nodes for beamforming in a 2-D plane.

This ensures that the nodes included in the calibration are within the desired baseline length. The number of active nodes is calculated as

$$N_{\text{active}} = \left\lfloor \frac{2\Delta\theta}{2\pi} N_{\text{node}} \right\rfloor. \quad (8)$$

Assuming isotropic sources and coherent summation, the ideal array gain is given by

$$G_{\text{ideal}} = 10 \log_{10} N_{\text{active}}^2. \quad (9)$$

C. Calibration Using Single Calibration Satellite (Satellite A)

In this calibration method, as shown in Fig. 7, a single calibration satellite (Satellite A) is used to send calibration signals to each node. The calibration process involves determining the relative phase delays between nodes based on the received calibration signals.

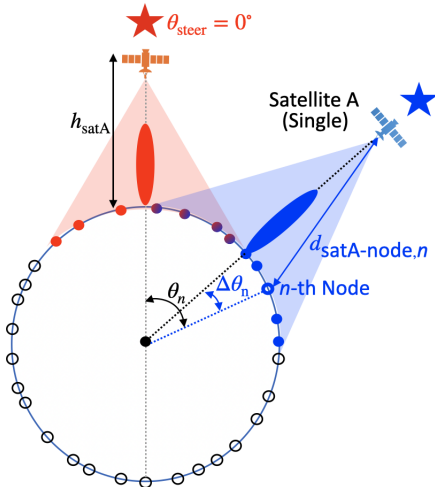


Fig. 7. Schematic for node calibration using single calibration satellite (Satellite A).

The distance between Satellite A and the n -th node is denoted as $d_{\text{satA-node},n}$, and the corresponding calibration phase shift is calculated by

$$\phi_{\text{cal,satA},n} = \frac{2\pi}{\lambda} d_{\text{satA-node},n}, \quad n = 1, 2, \dots, N_{\text{active}}. \quad (10)$$

We define the angular difference between each node and the steering direction as

$$\Delta\theta_n = \theta_{\text{steer}} - \theta_n, \quad (11)$$

where θ_n is the angular position of the n -th node.

The geometric phase term due to Earth's curvature is given by

$$\phi_{\text{geom,satA},n} = -\frac{2\pi}{\lambda} R_{\text{earth}} (1 - \cos \Delta\theta_n). \quad (12)$$

Assuming isotropic sources and applying uniform weighting, the array factor after calibration with Satellite A is

$$AF_{\text{satA}} = \sum_{n=1}^{N_{\text{active}}} \exp(j\phi_{\text{geom,satA},n} + j\phi_{\text{cal,satA},n}). \quad (13)$$

The array gain is calculated as the normalized magnitude squared of the array factor:

$$G_{\text{satA}} = 10 \log_{10} |AF_{\text{satA}}|^2. \quad (14)$$

In the far-field region (when the distance between Satellite A and Earth is large), the calibration phase $\phi_{\text{cal,satA},n}$ can be used to well compensate the geometric phase $\phi_{\text{geom,satA},n}$ variation among the nodes. In this case, the array gain G_{satA} is approximately equal to the ideal array gain G_{ideal} .

This calibration approach relies on a single satellite to receive astronomical signals from a specific direction. To achieve simultaneous multiple scanned beams, multiple satellites like Satellite A would be required. In sub-regions where the coverage of different satellites overlaps, like the overlap of red and blue sub-regions in Fig. 7, the calibration signals can be separated by employing different frequencies or coding schemes to avoid ambiguity.

D. Calibration Using Multiple Distributed Calibration Satellites (Satellite B)

To enhance the calibration process, we introduce multiple distributed calibration satellites (Satellite B) in Fig. 8. Each satellite in Satellite B is responsible for calibrating a specific sub-region of nodes. The direction from the center of each node sub-region to its corresponding satellite is aligned with the beam steering direction.

The angular positions of the satellites in Satellite B are defined as

$$\theta_{\text{satB},k} = -\pi + \left(k - \frac{1}{2}\right) \frac{2\pi}{N_{\text{satB}}}, \quad k = 1, 2, \dots, N_{\text{satB}}. \quad (15)$$

For the n -th node in the k -th sub-region, the calibration phase involves calculating the relative phase variation due

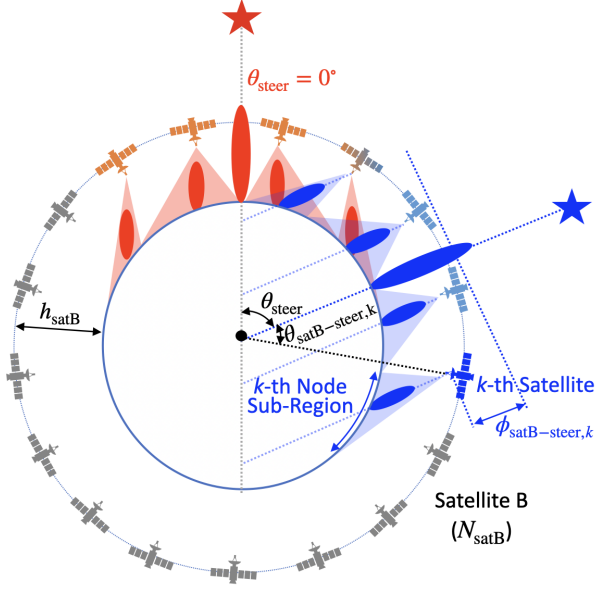


Fig. 8. Schematic for node calibration using multiple distributed calibration satellites (Satellite B).

different distance $d_{\text{satB-node},n}$ between the node and its corresponding satellite and relative phase $\phi_{\text{satB-ster},k}$ among each satellites. The calibration phase shift is

$$\phi_{\text{cal,satB},n} = \frac{2\pi}{\lambda} d_{\text{satB-node},n} + \phi_{\text{satB-ster},k}. \quad (16)$$

Here, $\phi_{\text{satB-ster},k}$ accounts for the phase difference between the k -th satellite and the plane wavefront in the steering direction, calculated by

$$\phi_{\text{satB-ster},k} = \frac{2\pi}{\lambda} (h_{\text{satB}} + R_{\text{earth}}) (1 - \cos \theta_{\text{satB-ster},k}), \quad (17)$$

where $\theta_{\text{satB-ster},k}$ is the angle difference between the k -th satellite and the steering direction:

$$\theta_{\text{satB-ster},k} = \theta_{\text{steer}} - \theta_{\text{satB},k}. \quad (18)$$

The geometric phase term for nodes due to Earth's curvature is

$$\phi_{\text{geom},n} = \frac{2\pi}{\lambda} R_{\text{earth}} \cos \Delta\theta_n. \quad (19)$$

Assuming isotropic sources and uniform weighting, the array factor after calibration with Satellite B is

$$AF_{\text{satB}} = \sum_{k=1}^{N_{\text{satB}}} \sum_{n \in \mathcal{R}_k} \exp(j\phi_{\text{geom},n} + j\phi_{\text{cal,satB},n}), \quad (20)$$

where \mathcal{R}_k represents the set of nodes in the k -th sub-region associated with the k -th satellite.

The array gain is then calculated as

$$G_{\text{satB}} = 10 \log_{10} (|AF_{\text{satB}}|^2). \quad (21)$$

As shown in Fig. 8, the satellites in Satellite B and the nodes can be multiplexed for different scanning beams. As the beam is steered, the node regions and corresponding satellites can be redefined, allowing for flexible beamforming capabilities.

E. Phase Error Mitigation Using GPS Localization

Unlike astronomical signals originating from sources at infinite distances, the finite distance of Satellite B introduces phase variations in the wavefront curvature across the array, leading to phase discrepancies among the nodes. To mitigate these phase errors, we employ GPS localization to estimate the positions of both the nodes and the satellites, allowing us to apply appropriate phase corrections during calibration.

Each node and satellite may have position estimation errors due to limitations in GPS accuracy. Let $\Delta_{\text{node,GPS}}$ and Δ_{sat} represent the maximum position errors for the nodes and satellites, respectively. The estimated positions are obtained by adding random errors within these bounds to the true positions.

For the n -th node with true position $(x_{\text{node},n}, z_{\text{node},n})$ in the k -th node sub-region, the estimated position is

$$\begin{aligned} x_{\text{node},n}^{\text{est}} &= x_{\text{node},n} + \delta x_{\text{node},n}, \\ z_{\text{node},n}^{\text{est}} &= z_{\text{node},n} + \delta z_{\text{node},n}, \end{aligned} \quad (22)$$

where $\delta x_{\text{node},n}$ and $\delta z_{\text{node},n}$ are random variables uniformly distributed in $[-\Delta_{\text{node,GPS}}, \Delta_{\text{node,GPS}}]$.

Similarly, the estimated position of the k -th satellite with true position $(x_{\text{satB},k}, z_{\text{satB},k})$ is

$$\begin{aligned} x_{\text{satB},k}^{\text{est}} &= x_{\text{satB},k} + \delta x_{\text{satB},k}, \\ z_{\text{satB},k}^{\text{est}} &= z_{\text{satB},k} + \delta z_{\text{satB},k}, \end{aligned} \quad (23)$$

where $\delta x_{\text{satB},k}$ and $\delta z_{\text{satB},k}$ are random variables uniformly distributed in $[-\Delta_{\text{sat}}, \Delta_{\text{sat}}]$. In practice, the satellite position can be estimated with an accuracy better than 1 centimeter [33]. Therefore, we can assume that the true satellite position is effectively known and set Δ_{sat} to zero.

Using the estimated positions, we calculate the estimated distance between each node and its corresponding satellite

$$d_{\text{satB-node},n}^{\text{est}} = \sqrt{(x_{\text{satB},k}^{\text{est}} - x_{\text{node},n}^{\text{est}})^2 + (z_{\text{satB},k}^{\text{est}} - z_{\text{node},n}^{\text{est}})^2}. \quad (24)$$

We also calculate the estimated radial distance of the node from Earth's center

$$r_{\text{node},n}^{\text{est}} = \sqrt{(x_{\text{node},n}^{\text{est}})^2 + (z_{\text{node},n}^{\text{est}})^2}. \quad (25)$$

The estimated angular positions of the node and satellite are

$$\begin{aligned} \theta_{\text{node},n}^{\text{est}} &= \arctan(x_{\text{node},n}^{\text{est}}, z_{\text{node},n}^{\text{est}}), \\ \theta_{\text{satB},k}^{\text{est}} &= \arctan(x_{\text{satB},k}^{\text{est}}, z_{\text{satB},k}^{\text{est}}). \end{aligned} \quad (26)$$

The estimated angle between the node and its corresponding satellite is

$$\Delta\theta_{\text{satB-node},n}^{\text{est}} = \theta_{\text{satB},k}^{\text{est}} - \theta_{\text{node},n}^{\text{est}}. \quad (27)$$

We compute an intermediate angle α_n using the Law of Sines

$$\alpha_n = \arcsin\left(\frac{r_{\text{node},n}^{\text{est}}}{d_{\text{satB-node},n}^{\text{est}}} \sin \Delta\theta_{\text{satB-node},n}^{\text{est}}\right). \quad (28)$$

The estimated angle between the satellite and the steering direction is

$$\Delta\theta_{\text{satB-ster},k}^{\text{est}} = \theta_{\text{steer}} - \theta_{\text{satB},k}^{\text{est}}. \quad (29)$$

The angle between the node-satellite line and the steering direction is then

$$\beta_n = \alpha_n - \Delta\theta_{\text{satB-steer},k}^{\text{est}}. \quad (30)$$

The excess path length due to the angle β_n is calculated by

$$\delta d_{\text{GPS},n} = d_{\text{satB-node},n}^{\text{est}} (1 - \cos \beta_n). \quad (31)$$

The GPS correction phase is then

$$\phi_{\text{GPS},n} = \frac{2\pi}{\lambda} \delta d_{\text{GPS},n}. \quad (32)$$

The corrected calibration phase for each node is

$$\phi_{\text{cal,GPS},n} = \phi_{\text{cal,satB},n} - \phi_{\text{GPS},n}, \quad (33)$$

where $\phi_{\text{cal,satB},n}$ is the original calibration phase without GPS correction, given by

$$\phi_{\text{cal,satB},n} = \frac{2\pi}{\lambda} d_{\text{satB-node},n} + \phi_{\text{satB-steer},k}. \quad (34)$$

The array factor after incorporating GPS-based correction is

$$AF_{\text{satB,GPS}} = \sum_{k=1}^{N_{\text{satB}}} \sum_{n \in \mathcal{R}_k} \exp(j\phi_{\text{geom},n} + j\phi_{\text{cal,GPS},n}). \quad (35)$$

The array gain with GPS correction is then

$$G_{\text{satB,GPS}} = 10 \log_{10} |AF_{\text{satB,GPS}}|^2. \quad (36)$$

In summary, the finite distance of Satellite B causes the incoming wavefront to have curvature, leading to phase discrepancies among the nodes when compared to plane wavefronts from astronomical sources at infinite distances. By using GPS estimates of the node and satellite positions, we calculate the angle between the node-satellite line and the steering direction, β_n . This angle results in an excess path length $\delta d_{\text{GPS},n}$, which introduces phase errors in the calibration process.

By computing $\delta d_{\text{GPS},n}$ and the corresponding correction phase $\phi_{\text{GPS},n}$, we adjust the calibration phase for each node to account for these errors, effectively aligning the phase of the received signals as if they were from an astronomical source at infinite distance.

F. Analysis Results for Calibration Using Satellite A

Fig. 9 illustrates the normalized array gain for Satellite A over different baseline lengths, with the satellite height h_{satA} varied among 10^6 meters, 10^8 meters, and 10^9 meters. The figure shows that the array gain decreases as the baseline length L_{baseline} increases. For a given baseline length, increasing the satellite height improves the array gain. This improvement is attributed to the reduction in wavefront curvature effects at higher altitudes, leading to more uniform phase fronts across the array. However, when the baseline length reaches 12×10^6 meters—approximately the diameter of the Earth—the required satellite height h_{satA} exceeds 10^9 meters to achieve acceptable array gain. Such altitudes are impractically large for real-world applications, highlighting the limitations of using a single calibration satellite for extensive baseline lengths.

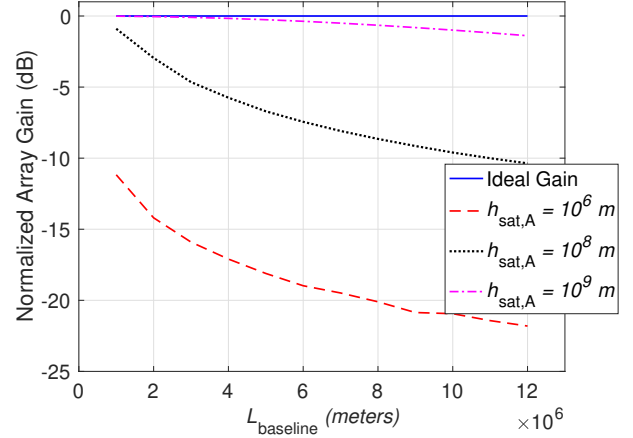


Fig. 9. Normalized array gain for Satellite A over different baseline lengths. The satellite heights are 10^6 m, 10^8 m, and 10^9 m.

G. Analysis Results for Calibration Using Satellite B

To address the limitations of the single-satellite calibration approach, we present analysis results for the proposed phase calibration method using Satellite B. The analysis explores various parameters such as node localization estimation error, steering angles, number of satellites, satellite heights, and baseline lengths.

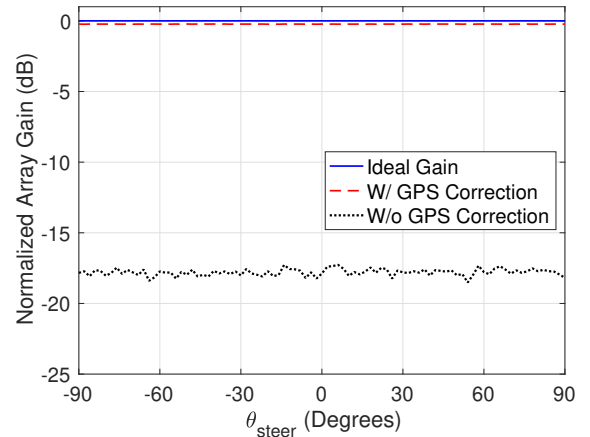


Fig. 10. Normalized array gain over different steering angles, with and without GPS correction.

1) *Effectiveness of GPS Correction:* Fig. 10 illustrates the normalized array gain over different steering angles, with and without GPS correction. The node localization estimation error with GPS $\Delta_{\text{node,GPS}}$ is set to 5 meters, the height of Satellite B is $h_{\text{satB}} = 5 \times 10^6$ meters, the baseline length is $L_{\text{baseline}} = 12,000$ kilometers, and the number of satellites is $N_{\text{satB}} = 1,000$.

The analysis results clearly demonstrate that GPS correction significantly enhances the array gain across all steering angles, achieving performance nearly equivalent to the ideal array gain G_{ideal} as defined in equation (9). In the absence of GPS correction, the array gain experiences a substantial degradation of over 18 dB, primarily due to phase errors introduced

by the wavefront curvature of Satellite B. GPS correction effectively mitigates these phase discrepancies by providing accurate position estimates, which ensures better alignment of the received signal phases and thereby restores the array gain to levels close to the ideal array gain.

2) *Impact of GPS Estimation Error:* Fig. 11 illustrates the normalized array gain for Satellite B as a function of GPS estimation error $\Delta_{\text{node,GPS}}$, with the number of satellites N_{satB} varied among 20, 100, and 1,000. The height of Satellite B is $h_{\text{satB}} = 5 \times 10^6$ meters, the baseline length is $L_{\text{baseline}} = 12,000$ kilometers, and the steering angle is $\theta_{\text{steer}} = 0^\circ$.

The results clearly show that the array gain decreases as the GPS estimation error increases. This degradation occurs because larger estimation errors in the node positions lead to less effective correction of the curvature of the satellite calibration signal's wavefront. As a result, the phases of the received signals become misaligned, leading to less coherent combining and a reduction in array gain.

For a given GPS estimation error $\Delta_{\text{node,GPS}}$, increasing the number of satellites N_{satB} enhances the array gain. This improvement can be explained by the fact that increasing the number of satellites divides the array into more node sub-regions, each calibrated by its own satellite. This division effectively reduces the baseline length within each node sub-region. As observed from the results in Fig. 9, a smaller baseline length corresponds to a larger array gain due to reduced phase errors over shorter distances. Therefore, increasing N_{satB} mitigates the adverse effects of GPS estimation errors by limiting phase discrepancies within smaller sub-arrays. This enhancement is especially noticeable when the GPS estimation error is relatively large, as the impact of position inaccuracies is confined within smaller regions, allowing for more effective phase alignment and improved overall array performance.

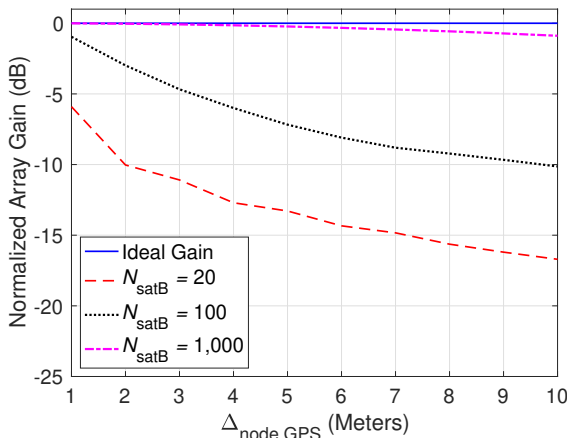


Fig. 11. Normalized array gain with different GPS estimation errors $\Delta_{\text{node,GPS}}$.

3) *Impact of Beam Steering Angles:* Fig. 12 presents the normalized array gain for Satellite B as a function of steering angle θ_{steer} , with the number of satellites N_{satB} varied among 20, 50, and 500. In this analysis, the node localization estimation error with GPS is set to $\Delta_{\text{node,GPS}} = 5$ meters, the

height of Satellite B is $h_{\text{satB}} = 5 \times 10^6$ meters, and the baseline length is $L_{\text{baseline}} = 12,000$ kilometers.

When $N_{\text{satB}} = 20$, the array gain is over 13 dB less than the ideal array gain at certain steering angles. The dips in the array gain as θ_{steer} varies are due to significant phase errors when the beam is steered between the coverage areas of adjacent satellites.

As the number of satellites increases to $N_{\text{satB}} = 50$, the ripple effect is mitigated, and the array gain improves across the steering angle range. This is because the additional satellites provide better coverage and reduce the gaps between calibration regions, resulting in more consistent scanned beams.

When N_{satB} is further increased to 500, the array gain becomes almost identical to the ideal array gain and remains nearly constant across all steering angles θ_{steer} . The high density of satellites ensures continuous scanned beams, effectively eliminating phase errors due to satellite transitions.

These results indicate that by sufficiently increasing the number of calibration satellites, the proposed telescope system can achieve a nearly isotropic gain response. Moreover, theoretically, an infinite number of beams with uniform gain over the full scan range can be implemented simultaneously using digital beamforming techniques. This represents a significant improvement over traditional radio telescopes, which are typically limited to only up to tens of simultaneous beams [34].

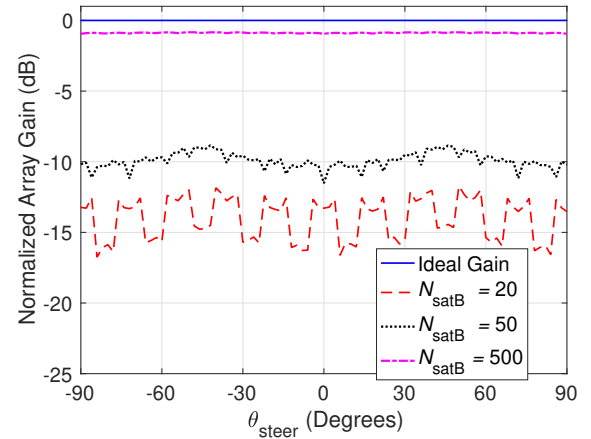


Fig. 12. Normalized array gain with different steering angles for various numbers of satellites.

4) *Impact of Number of Satellites:* Fig. 13 depicts the normalized array gain for Satellite B with different numbers of satellites N_{satB} . The satellite heights h_{satB} are 1×10^6 m, 5×10^6 m, and 2×10^7 m. The node localization estimation error with GPS is set to $\Delta_{\text{node,GPS}} = 5$ meters, the baseline length is $L_{\text{baseline}} = 12,000$ kilometers, and the steering angle is $\theta_{\text{steer}} = 0^\circ$.

The results indicate that for a given satellite height, increasing the number of satellites enhances the array gain. Moreover, higher satellite altitudes result in better performance due to reduced wavefront curvature effects. This demonstrates that both the number of satellites and their altitude play crucial roles in achieving optimal array gain.

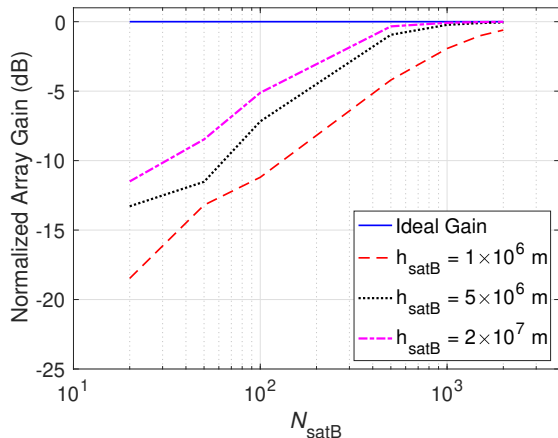


Fig. 13. Normalized array gain with different numbers of satellites at various satellite heights.

5) *Impact of Satellite Height:* Fig. 14 illustrates the normalized array gain for Satellite B over different satellite heights h_{satB} , with the number of satellites N_{satB} varied among 20, 100, and 500. The node localization estimation error with GPS is set to $\Delta_{\text{node,GPS}} = 5$ meters, the baseline length is $L_{\text{baseline}} = 12,000$ kilometers, and the steering angle is $\theta_{\text{steer}} = 0^\circ$.

The array gain improves with increasing satellite height due to the flattening of the wavefronts at higher altitudes. This effect is more pronounced when combined with a higher number of satellites, which further reduces phase errors due to the smaller baselines of the node sub-regions.

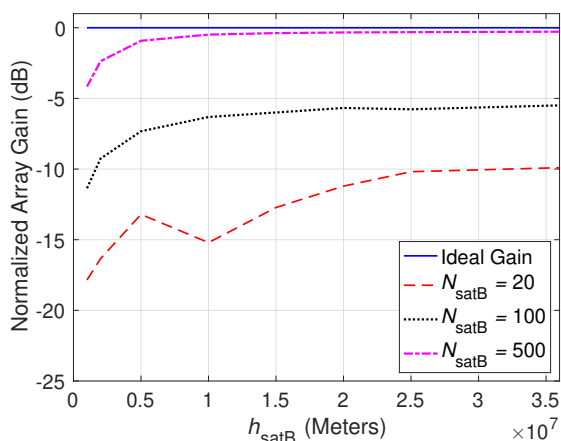


Fig. 14. Normalized array gain over different satellite heights for various numbers of satellites.

6) *Impact of Baseline Length:* Fig. 15 shows the normalized array gain for Satellite B over different baseline lengths L_{baseline} , with the number of satellites N_{satB} set to 50, 100, and 500. The node localization estimation error with GPS is set to $\Delta_{\text{node,GPS}} = 5$ meters, the satellite height is $h_{\text{satB}} = 5 \times 10^6$ meters, and the steering angle is $\theta_{\text{steer}} = 0^\circ$. The results indicate that as the baseline length increases, the array gain increased due to increased number of nodes. Increasing the

number of satellites helps mitigate this degradation from the ideal gain by providing more precise phase calibration over the extended baseline.

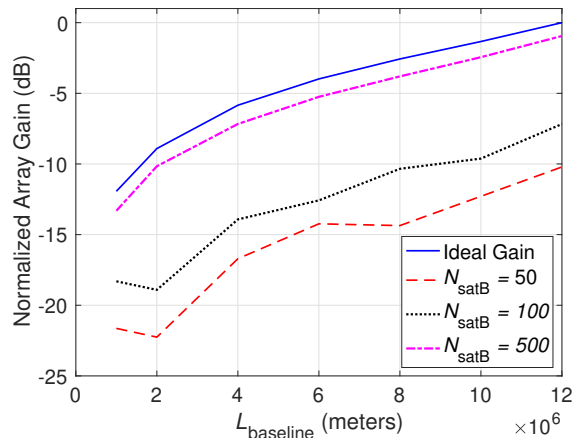


Fig. 15. Normalized array gain over different baseline lengths for various numbers of satellites.

H. Summary

In summary, the analysis results validate the effectiveness of the proposed phase calibration method using multiple distributed calibration satellites (Satellite B) with GPS localization. Key findings include:

- *Proposed Multi-Satellite Calibration with GPS Correction:* Employing multiple distributed calibration satellites (Satellite B) combined with GPS localization effectively addresses the limitations of single-satellite calibration by mitigating phase errors and enhancing array performance.
- *Effectiveness of GPS Correction:* GPS localization significantly enhances the array gain by correcting phase errors arising from position uncertainties and the finite distances of calibration satellites. This correction brings the array's performance close to the ideal case, ensuring accurate phase alignment across the array.
- *Impact of Number of Satellites:* Increasing the number of calibration satellites improves the array gain, especially over longer baseline lengths. A larger number of satellites reduces phase errors associated with wavefront curvature and node position inaccuracies by dividing the array into smaller, more manageable sub-regions.
- *Benefits of Higher Satellite Altitudes:* Deploying satellites at higher altitudes reduces wavefront curvature effects, leading to improved array gain. This benefit is amplified when combined with a larger number of satellites, as the flatter wavefronts enhance phase alignment across the array.
- *Baseline Length Considerations:* Although longer baseline lengths introduce more significant phase errors, these can be effectively mitigated by increasing both the number of satellites and their altitudes, along with utilizing GPS correction.
- *Enhanced Beamforming Capabilities:* This method facilitates a nearly isotropic gain response continuously

over the full scanning range. It enables the simultaneous implementation of infinite beams in theory using digital beamforming techniques, surpassing the limitations of traditional radio telescopes that are typically restricted to a limited number of simultaneous beams.

These results underscore the potential of the proposed calibration method for practical applications requiring precise beamforming and high-resolution imaging in large-scale distributed arrays.

IV. CALIBRATION METHOD PERFORMANCE UNDER NODE VARIABILITY

In this section, we analyze and compare the performance of two calibration methods for large-scale distributed arrays in the presence of variability in node gains due to different path losses and system noise figures at each node. The methods under consideration are the *Phase Alignment Calibration* and the *Eigenvalue-Based Calibration*. We present a detailed mathematical model and discuss the implications of the results.

A. System Model

We consider a linear array of N nodes distributed along the x -axis over a total aperture length L . The nodes receive both a strong calibration signal and a weak astronomical signal. Each node is equipped with a receiver characterized by an antenna gain G_n and a noise figure NF_n , which exhibit variability to simulate real-world hardware inconsistencies.

The key signal parameters include the center frequency f_c , the wavelength $\lambda_c = c/f_c$ (where c is the speed of light), the bandwidth B , the calibration signal power density P_{cal} , and the astronomical signal power density P_{astro} .

The positions of the nodes are given by

$$x_n = L \times (u_n - 0.5), \quad (37)$$

where u_n is a uniform random variable over $[0, 1]$, representing the random distribution of nodes along the array.

The antenna gains G_n can vary due to different blockage effects at each node and are expressed in decibels (dB) as

$$G_n^{\text{dB}} = \overline{G}_{\text{ant}} + \sigma_G z_n^{(G)}, \quad (38)$$

where $\overline{G}_{\text{ant}}$ is the mean antenna gain in dB, σ_G is the standard deviation, and $z_n^{(G)}$ is a standard normal random variable.

Similarly, the noise figures NF_n (in dB) are modeled as

$$NF_n^{\text{dB}} = \overline{NF} + \sigma_{NF} z_n^{(NF)}, \quad (39)$$

where \overline{NF} is the mean noise figure in dB, σ_{NF} is the standard deviation, and $z_n^{(NF)}$ is a standard normal random variable.

The effective antenna area for the n -th node is calculated using

$$A_{\text{eff},n} = \frac{G_n \lambda_c^2}{4\pi}, \quad (40)$$

where G_n is the linear antenna gain.

The noise power at the n -th node is given by

$$P_{\text{noise},n} = k_B T_{\text{noise},n} B, \quad (41)$$

where k_B is the Boltzmann constant, B is the bandwidth, and the noise temperature $T_{\text{noise},n}$ is

$$T_{\text{noise},n} = T_0 \times NF_n, \quad (42)$$

with T_0 being the reference temperature (290 K) and NF_n is the noise figure in linear scale.

The direction of arrival (DoA) for the astronomical signal is denoted by θ_s , and the wave number is

$$k_c = \frac{2\pi}{\lambda_c}. \quad (43)$$

The total calibration time is denoted by T_{cal} , which is divided into a calibration-on duration $T_{\text{cal-on}}$ (when the calibration signal is present) and a calibration-off duration $T_{\text{cal-off}} = T_{\text{cal}} - T_{\text{cal-on}}$ (when the calibration signal is absent). The observation time is denoted by T_{obs} .

The received signals at each node consist of the desired signal and additive noise. The variability in antenna gains and noise figures among the nodes introduces differences in the received signal amplitudes and noise levels, which the calibration methods aim to compensate for.

B. Signal Model

During the calibration-on period, the received calibration signal at node n is

$$s_n^{\text{cal-on}}(t) = A_n^{\text{cal}} \cos(2\pi f_c t - k_c x_n \cos \theta_{\text{cal}}), \quad (44)$$

where $A_n^{\text{cal}} = \sqrt{2P_{\text{cal}}A_{\text{eff},n}}$ is the amplitude, $A_{\text{eff},n}$ is the effective antenna area, and θ_{cal} is the known calibration signal's DoA.

During the observation period, the received astronomical signal at node n is

$$s_n^{\text{obs}}(t) = A_n^{\text{obs}} \cos(2\pi f_c t - k_c x_n \cos \theta_s), \quad (45)$$

where $A_n^{\text{obs}} = \sqrt{2P_{\text{astro}}A_{\text{eff},n}}$.

The noise at node n is modeled as zero-mean Gaussian noise with variance $\sigma_n^2 = P_{\text{noise},n}$:

$$n_n(t) \sim \mathcal{N}(0, \sigma_n^2). \quad (46)$$

The received signals at each node are the sum of the desired signal and the noise:

$$r_n(t) = s_n(t) + n_n(t), \quad (47)$$

where $s_n(t)$ represents either the calibration signal or the astronomical signal, depending on the time period.

C. Calibration Methods

We compare two calibration methods: Phase Alignment Calibration and Eigenvalue-Based Calibration.

1) *Phase Alignment Calibration (PAC)*: In the Phase Alignment Calibration method, the relative phase differences between nodes are estimated and compensated using cross-correlation during the calibration-on period. After downconversion and low-pass filtering, the baseband signal at node n during calibration-on is

$$y_n^{\text{cal-on}}(t) = A_n^{\text{cal}} e^{-jk_c x_n \cos \theta_{\text{cal}}} + \tilde{n}_n^{\text{cal-on}}(t), \quad (48)$$

where $\tilde{n}_n^{\text{cal-on}}(t)$ is the baseband noise.

The phase difference between node n and a reference node (chosen as node 1) is estimated as

$$\hat{\Delta\phi}_n = \arg \left\{ \frac{1}{T_{\text{cal-on}}} \int_0^{T_{\text{cal-on}}} y_n^{\text{cal-on}}(t) (y_1^{\text{cal-on}}(t))^* dt \right\}. \quad (49)$$

The beamforming weights are then calculated as

$$w_n = e^{-j\hat{\Delta\phi}_n}. \quad (50)$$

During observation, the weighted signals are combined to form the array output:

$$y_{\text{combined}}^{\text{PAC}}(t) = \sum_{n=1}^N w_n y_n^{\text{obs}}(t), \quad (51)$$

where $y_n^{\text{obs}}(t)$ is the baseband astronomical signal at node n after downconversion and filtering.

2) *Eigenvalue-Based Calibration (EVC)*: In this method, optimal beamforming weights are computed by solving a generalized eigenvalue problem using covariance matrices estimated during calibration.

The noise covariance matrix \mathbf{R}_n is estimated during the calibration-off period:

$$\mathbf{R}_n = \frac{1}{T_{\text{cal-off}}} \int_0^{T_{\text{cal-off}}} \mathbf{y}^{\text{cal-off}}(t) \mathbf{y}^{\text{cal-off}}(t)^\dagger dt, \quad (52)$$

where $\mathbf{y}^{\text{cal-off}}(t) = [y_1^{\text{cal-off}}(t), \dots, y_N^{\text{cal-off}}(t)]^\top$ and \dagger denotes the Hermitian transpose.

Similarly, the signal-plus-noise covariance matrix \mathbf{R}_{sn} is estimated during the calibration-on period:

$$\mathbf{R}_{\text{sn}} = \frac{1}{T_{\text{cal-on}}} \int_0^{T_{\text{cal-on}}} \mathbf{y}^{\text{cal-on}}(t) \mathbf{y}^{\text{cal-on}}(t)^\dagger dt. \quad (53)$$

The signal covariance matrix is obtained by subtracting the noise covariance from the signal-plus-noise covariance:

$$\mathbf{R}_s = \mathbf{R}_{\text{sn}} - \mathbf{R}_n. \quad (54)$$

The optimal weights \mathbf{w} are determined by solving the generalized eigenvalue problem:

$$\mathbf{R}_s \mathbf{w} = \lambda_{\text{max}} (\mathbf{R}_n + \epsilon \mathbf{I}) \mathbf{w}, \quad (55)$$

where ϵ is a regularization parameter to prevent numerical issues (set as $\epsilon = \varepsilon \cdot \text{trace}(\mathbf{R}_n)/N$ with ε being a small constant), \mathbf{I} is the identity matrix, and λ_{max} is the largest eigenvalue.

The eigenvector corresponding to the largest eigenvalue λ_{max} is selected as the optimal weight vector. The weights are normalized to maintain consistent array gain:

$$\mathbf{w}_{\text{norm}} = \frac{\mathbf{w}}{\left(\sum_{n=1}^N |w_n| \right) / N}. \quad (56)$$

During observation, the signals are combined using the conjugate of the normalized weights:

$$y_{\text{combined}}^{\text{EVC}}(t) = \mathbf{y}^{\text{obs}}(t)^\dagger \mathbf{w}_{\text{norm}}^*, \quad (57)$$

where $\mathbf{y}^{\text{obs}}(t) = [y_1^{\text{obs}}(t), \dots, y_N^{\text{obs}}(t)]^\top$ and $*$ denotes complex conjugation.

D. SNR Calculation

For both methods, the array output SNR is calculated as

$$\text{SNR} = \frac{P_s}{P_n}, \quad (58)$$

where P_s is the total signal power, and P_n is the total noise power at the array output.

The total signal power is computed as

$$P_s = \left| \int_0^{T_{\text{obs}}} y_{\text{combined}}(t) dt \right|^2. \quad (59)$$

The total noise power is estimated using the variance of the combined noise-only signals:

$$P_n = \sigma_{\text{combined}}^2 \cdot T_{\text{obs}}, \quad (60)$$

where $\sigma_{\text{combined}}^2$ is the variance of $y_{\text{combined}}(t)$ when only noise is present.

E. Analysis Results

We simulate the performance of both calibration methods under two different scenarios:

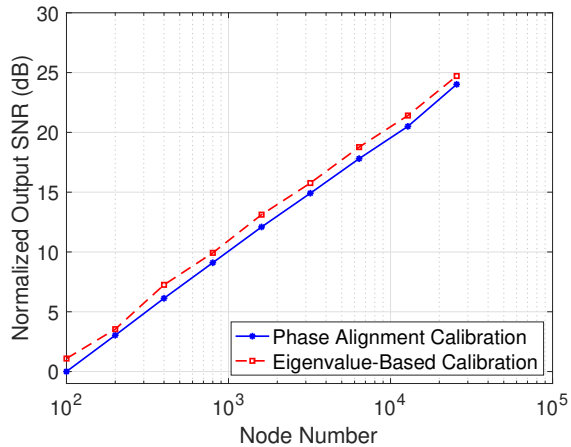
1. *Uniform Node Characteristics*: In this scenario, all nodes have identical antenna gains and noise figures, meaning there is no variability among the nodes ($\sigma_G = 0$ dB and $\sigma_{NF} = 0$ dB). This represents an ideal case with no hardware inconsistencies.

2. *Variable Node Characteristics*: In this scenario, nodes exhibit significant variability in antenna gains and noise figures, as previously described, with $\sigma_G = 20$ dB and $\sigma_{NF} = 4$ dB. This simulates real-world conditions where variations in hardware and antenna blockage effects for receiver nodes are present.

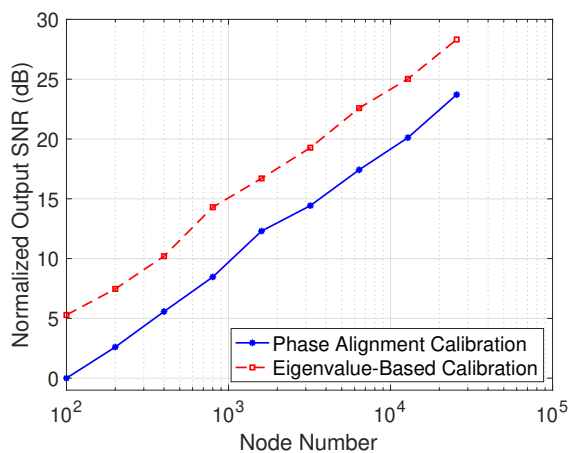
For both scenarios, we vary the number of nodes N from 100 to 25,600. The other analysis parameters are consistent across both scenarios: total array length $L = 1,000$ km; center frequency $f_c = 1.42$ GHz; bandwidth $B = 10$ kHz; calibration signal power density $P_{\text{cal}} = 10^{-10}$ W/m²; astronomical signal power density $P_{\text{astro}} = 10^{-20}$ W/m²; mean antenna gain $\bar{G}_{\text{ant}} = -10$ dB; mean noise figure $\bar{NF} = 4$ dB; calibration time $T_{\text{cal}} = 1$ ms (with $T_{\text{cal-on}} = T_{\text{cal}}/2$); observation time $T_{\text{obs}} = 1$ ms; reference temperature $T_0 = 290$ K; regularization parameter $\varepsilon = 10^{-3}$.

The array output SNRs for both methods under the two scenarios are plotted in Fig. 16, where Fig. 16(a) corresponds to the uniform node characteristics and Fig. 16(b) corresponds to the variable node characteristics.

In the uniform node scenario shown in Fig. 16(a), both methods achieve similar array output SNRs across all values of N . This indicates that when the nodes are identical, the simpler PAC method is sufficient to achieve near-optimal performance.



(a)



(b)

Fig. 16. Array output SNR versus the number of nodes for Phase Alignment Calibration (PAC) and Eigenvalue-Based Calibration (EVC) under (a) uniform node characteristics and (b) variable node characteristics.

In contrast, in the variable node scenario depicted in Fig. 16(b), the EVC method consistently outperforms the PAC method, demonstrating that EVC scales better with larger arrays under conditions of hardware variability.

Fig. 17 illustrates the array output SNR as a function of the standard deviation of the node gain, σ_G . The EVC method consistently achieves higher output SNR than the PAC method. Moreover, the performance gap between the two methods widens as the gain variation increases, indicating that the EVC method is more robust to variations in node gain.

F. Discussion

The analysis results highlight the impact of node variability on the performance of the two calibration methods. When antenna gains and noise figures are uniform across all nodes, both PAC and EVC methods effectively combine the signals coherently. In this ideal scenario, the simpler PAC method achieves near-optimal performance while requiring less computational resources and simpler hardware implementation.

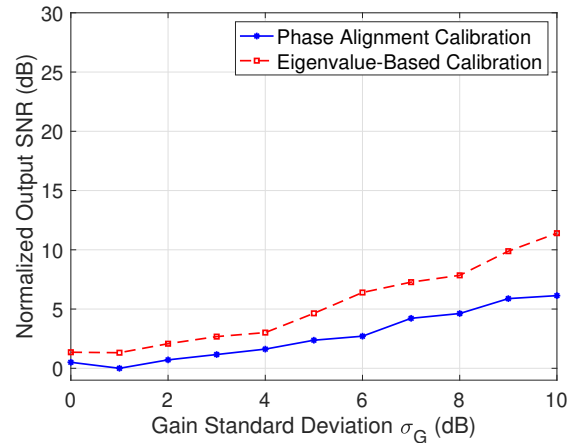


Fig. 17. Comparison of array output SNR versus standard deviation of node gain σ_G for the Eigenvalue-Based Calibration EVC and Phase Alignment Calibration PAC methods.

This makes the PAC method attractive for systems with limited resources and consistent node characteristics.

However, in practical applications such as IoT-enabled telescopes, nodes often exhibit significant variability in antenna gains and noise figures due to environmental factors like building obstructions, terrain variations, and differing hardware components. These variations lead to discrepancies in signal amplitudes and noise levels across the array. The PAC method, which assumes equal contribution from all nodes after phase alignment, neglects these differences, resulting in degraded performance when nodes have varying SNRs.

The EVC method, on the other hand, optimally adjusts both the phase and amplitude of the beamforming weights based on individual node characteristics by solving a generalized eigenvalue problem. This approach emphasizes nodes with higher SNRs and attenuates contributions from noisier nodes, effectively mitigating the adverse effects of hardware variability. Consequently, the EVC method achieves higher array output SNR and demonstrates better scalability and robustness for large arrays with hardware imperfections.

Considering the advantages and limitations of both methods, a hybrid approach can be beneficial in practical deployments. In environments where nodes have similar output SNRs, such as outdoor and open areas with minimal obstructions, the PAC method can be employed to capitalize on its simplicity and lower resource requirements. In urban areas or regions with significant node gain and noise figure variations due to obstructions or hardware differences, the EVC method becomes essential to ensure optimal performance.

By classifying nodes based on their SNR characteristics and applying the appropriate calibration method, the system can efficiently utilize resources while maintaining high performance. This adaptive approach leverages the strengths of both methods, providing a practical solution for large-scale distributed arrays in diverse environments.

V. ROUGH PERFORMANCE ESTIMATION AND COMPARATIVE ANALYSIS

This section presents a comparative analysis of the proposed IoT-based radio telescope and the Green Bank Telescope (GBT), focusing on key performance metrics such as antenna gain, system noise temperature, sensitivity, field of view (FoV), bandwidth, beamwidth, and survey speed. The aim is to evaluate the potential of the IoT telescope concept relative to a state-of-the-art radio telescope.

A. Performance Metrics

The performance parameters considered for comparison include the antenna gain (G), which represents the gain in the sky direction and incorporates the antenna radiation efficiency (η_{rad}) and blockage effects (L_{path}) due to environmental obstacles like buildings and trees. The system noise temperature (T_{sys}) accounts for the total noise from both the environment and the receiver electronics. Sensitivity (S) is defined as $S = G/T_{\text{sys}}$, indicating the ability to detect weak signals. The field of view (FoV) is the angular area over which the telescope can detect signals, approximated by $\text{FoV} = N_{\text{effb}}(\lambda/D)^2$, where N_{effb} is the number of effective beams, λ is the wavelength, and D is the diameter of the telescope. Beamwidth (θ_{bw}) is given by $\theta_{\text{bw}} \approx \lambda/D$, representing the angular width of the main lobe of the antenna pattern. Bandwidth (B) is the frequency range over which the telescope operates. Survey speed (SS) is calculated as $\text{SS} = BS^2\text{FoV}$, reflecting the speed at which the telescope can survey the sky.

B. Green Bank Telescope Parameters

For the Green Bank Telescope (GBT), we consider a diameter of $D_{\text{GBT}} = 100$ m and an aperture efficiency of $\eta_{\text{ap}} = 0.6$, as reported in [34]. The system noise temperature is $T_{\text{sys,GBT}} = 15$ K, and it operates over a bandwidth of $B_{\text{GBT}} = 300$ MHz. Operating at a wavelength of $\lambda = 0.21$ m, the GBT utilizes $N_{\text{effb}} = 25$ effective beams.

Using these parameters, the antenna gain of the GBT is calculated as $G_{\text{GBT}} = (4\pi\eta_{\text{ap}}A_{\text{GBT}})/\lambda^2$, where A_{GBT} is the reflector aperture area. The beamwidth is approximated by $\theta_{\text{bw,GBT}} \approx \lambda/D_{\text{GBT}}$, and the field of view is determined by $\text{FoV}_{\text{GBT}} = N_{\text{effb}}\theta_{\text{bw,GBT}}^2$.

C. Proposed IoT Telescope Parameters

A rough estimation of the proposed IoT-based radio telescope's performance metrics can be derived from various front-end figures of merit. The antenna directivity D_{IoT} for an individual IoT device is set at 0 dB, implying that these antennas are compact and designed to radiate power uniformly in all directions. The total antenna efficiency, encompassing radiation efficiency η_{rad} and impedance matching, is approximately -6 dB [35], [36], aligning with the efficiency typically observed in cellular phone antennas.

The average signal propagation loss L_{path} due to building blockages is estimated at 10 dB, reflecting the attenuation typically experienced from indoor to outdoor environments, such as GPS signal loss [37]–[39]. Given the omnidirectional

radiation patterns of most single-antenna IoT devices, the external environmental noise temperature interfacing with the IoT receivers is expected to be around 300 K. The RF front-end noise temperature is primarily influenced by the first-stage Low Noise Amplifier (LNA), which typically has a noise temperature of about 100 K, representative of commercial LNAs used in consumer electronics [40]. Since the receiver output SNR for most astronomical signals is below 0 dB, implementing a threshold near the receiver's noise floor can suppress interference from stronger communication signals. This strategic processing enables the network to treat interference from communication signals as background noise, which can subsequently be removed from the final data output.

The system's operational bandwidth is projected to be 300 MHz at a center frequency of 1.4 GHz. With an estimated $N_{\text{IoT}} = 1 \times 10^{12}$ global IoT devices contributing to the beamforming process [11]. The individual device antenna gain at the sky direction is calculated as $G_{\text{IoT}} = D_{\text{IoT}}L_{\text{path}}\eta_{\text{rad}}$. Multiplying by the number of devices, the cumulative antenna gain is $G_{\text{IoT,total}} = G_{\text{IoT}}N_{\text{IoT}}/2$.

The beamwidth of the IoT telescope is approximated by $\theta_{\text{bw,IoT}} \approx \lambda/D_{\text{Earth}}$, where $D_{\text{Earth}} \approx 12,742$ km is the Earth's diameter. This results in an extremely narrow beamwidth due to the large effective aperture size. The field of view for the IoT telescope is considered to be $\text{FoV}_{\text{IoT}} = 2\pi$, covering the entire visible hemisphere to avoid interference from sunlight.

TABLE I
COMPARISON OF THE PROPOSED IoT TELESCOPE WITH THE GBT

Parameter	GBT	IoT Telescope
Antenna Gain (G)	61.2 dB	94.0 dB
Noise Temperature (T_{sys})	15 K	400 K
Sensitivity ($S = G/T_{\text{sys}}$)	$8.86 \times 10^4 \text{ K}^{-1}$	$3.13 \times 10^6 \text{ K}^{-1}$
Beamwidth (θ_{bw})	$2.11 \times 10^{-3} \text{ sr}$	$1.66 \times 10^{-8} \text{ sr}$
Field of View (FoV)	$1.12 \times 10^{-4} \text{ sr}$	$2\pi \text{ sr}$
Bandwidth (B)	300 MHz	300 MHz
Survey Speed (SS)	2.62×10^{14}	1.84×10^{22}

D. Performance Comparison Table

Table I summarizes the key performance metrics based on the above analysis. Despite each individual IoT device having a low antenna gain, the cumulative effect of aggregating signals from an immense number of devices results in a total antenna gain that is over three orders of magnitude higher than that of the GBT. This significant increase is due to the vast number of participating IoT devices in the network. The system noise temperature of the IoT telescope is higher because IoT devices typically have greater noise figures, and the external environmental noise temperature is approximately equal to room temperature (300 K). However, the IoT telescope offers a vastly larger field of view, effectively covering almost the entire sky simultaneously. In contrast, the GBT has a much smaller FoV due to its highly directional reflector antenna. Consequently, the IoT telescope achieves a survey speed that is nearly eight orders of magnitude greater than that of the GBT, attributed to the large number of nodes and the expansive FoV.

VI. CONCLUSION

This paper presents a novel approach to radio astronomy by leveraging the global network of IoT devices to form a large-scale, distributed radio telescope. The proposed system addresses the limitations of traditional radio telescopes in spectrum sharing and operational environments by utilizing widely dispersed IoT devices capable of concurrent astronomical and communication signal reception. Through digital beamforming techniques and the implementation of calibration methods using multiple distributed satellites with GPS localization, the system effectively mitigates phase errors and hardware inconsistencies among nodes.

Analysis results demonstrate that the Eigenvalue-Based Calibration (EVC) method outperforms the Phase Alignment Calibration (PAC) method in environments with significant node variability, highlighting the importance of optimal weight adjustments based on individual node characteristics. The comparative performance analysis with the Green Bank Telescope (GBT) underscores the potential advantages of the IoT-based telescope, particularly in terms of increasing antenna gain by three orders of magnitude and enhancing survey speed by eight orders of magnitude.

The findings indicate that the IoT-enabled radio telescope concept is not only feasible but also offers substantial benefits over traditional systems. By capitalizing on existing infrastructure and advancements in connectivity, the proposed system paves the way for cost-effective, high-speed, and widely accessible astronomical observations.

REFERENCES

- [1] How much would it cost to clear out the defunct arecibo radio telescope and rebuild it? the location seems ideal for a large radio telescope. [Online]. Available: <https://www.quora.com/>
- [2] [Online]. Available: <https://futurism.com/the-quest-for-life-beyond-earth-the-worlds-largest-radio-telescope-just-went-online>
- [3] R. C. Hansen, "Fundamental limitations in antennas," *Proceedings of the IEEE*, vol. 69, no. 2, pp. 170–182, 1981.
- [4] W. Davis, T. Yang, E. Caswell, and W. Stutzman, "Fundamental limits on antenna size: a new limit," *IET microwaves, antennas & propagation*, vol. 5, no. 11, pp. 1297–1302, 2011.
- [5] W. Geyi, "Physical limitations of antenna," *IEEE Transactions on Antennas and Propagation*, vol. 51, no. 8, pp. 2116–2123, 2003.
- [6] K. I. Kellermann, E. N. Bouton, S. S. Brandt, K. I. Kellermann, E. N. Bouton, and S. S. Brandt, "Nrao and radio astronomy in the twenty-first century," *Open Skies: The National Radio Astronomy Observatory and Its Impact on US Radio Astronomy*, pp. 583–614, 2020.
- [7] Z. Z. Abidin, Z. Rosli, M. S. Radzi, N. M. Shah, M. Dahari, F. Ramadhani, M. I. Ghazali, B. Azarbad, U. F. Ibrahim, and N. Hashim, "Radio quiet and radio notification zones characteristics for radio astronomy in medium densely populated areas and humid tropical countries," *Journal of Astronomical Telescopes, Instruments, and Systems*, vol. 7, no. 2, pp. 027001–027001, 2021.
- [8] K. I. Kellermann, E. N. Bouton, S. S. Brandt, K. I. Kellermann, E. N. Bouton, and S. S. Brandt, "The largest feasible steerable telescope," *Open Skies: The National Radio Astronomy Observatory and Its Impact on US Radio Astronomy*, pp. 461–531, 2020.
- [9] C. Beaudet, J. Ford, T. Minter, M. McCarty, K. O'Neil, and R. Prestage, "Radio frequency interference management efforts at the national radio astronomy observatory green bank site," in *2013 US National Committee of URSI National Radio Science Meeting (USNC-URSI NRSM)*. IEEE, 2013, pp. 1–1.
- [10] W. A. Sizemore, "The national radio quiet zone and the green bank rfi environment," in *International Astronomical Union Colloquium*, vol. 112. Cambridge University Press, 1991, pp. 176–180.
- [11] G. Karunarathne, K. Kulawansa, and M. Firdhous, "Wireless communication technologies in internet of things: A critical evaluation," in *2018 International conference on intelligent and innovative computing applications (ICONIC)*. IEEE, 2018, pp. 1–5.
- [12] "https://futuretimeline.net/data-trends/2050-future-internet-speed-predictions.htm."
- [13] "https://futuretimeline.net/data-trends/6.htm."
- [14] P. Jaroenjittichai, S. Punyawarin, D. Singwong, P. Somboonpon, N. Prasert, K. Bandudej, P. Kempet, A. Leckngam, S. Poshyachinda, B. Soonthornthum *et al.*, "Radio frequency interference site survey for thai radio telescopes," in *Journal of Physics: Conference Series*, vol. 901, no. 1. IOP Publishing, 2017, p. 012062.
- [15] W. Baan, P. Fridman, and R. Millenaar, "Radio frequency interference mitigation at the westerbork synthesis radio telescope: Algorithms, test observations, and system implementation," *The Astronomical Journal*, vol. 128, no. 2, p. 933, 2004.
- [16] P. Bolli, F. Gaudiomonte, R. Ambrosini, C. Bortolotti, M. Roma, C. Barberi, and F. Piccoli, "The mobile laboratory for radio-frequency interference monitoring at the sardinia radio telescope," *IEEE Antennas and Propagation Magazine*, vol. 55, no. 5, pp. 19–24, 2013.
- [17] F. Briggs, J. Bell, and M. Kesteven, "Removing radio interference from contaminated astronomical spectra using an independent reference signal and closure relations," *The Astronomical Journal*, vol. 120, no. 6, p. 3351, 2000.
- [18] M. Kesteven, "Radio-frequency interference mitigation in radio astronomy," *URSI Radio Science Bulletin*, vol. 2007, no. 322, pp. 9–18, 2007.
- [19] A. Leshem, A.-J. van der Veen, and A.-J. Boonstra, "Multichannel interference mitigation techniques in radio astronomy," *The Astrophysical Journal Supplement Series*, vol. 131, no. 1, p. 355, 2000.
- [20] F. H. Briggs and J. Kocz, "Overview of technical approaches to radio frequency interference mitigation," *Radio Science*, vol. 40, no. 05, pp. 1–11, 2005.
- [21] P. Fridman and W. Baan, "Rfi mitigation methods in radio astronomy," *Astronomy & Astrophysics*, vol. 378, no. 1, pp. 327–344, 2001.
- [22] N. Bhat, J. Cordes, S. Chatterjee, and T. Lazio, "Radio frequency interference identification and mitigation using simultaneous dual-station observations," *Radio Science*, vol. 40, no. 05, pp. 1–16, 2005.
- [23] T. An, X. Chen, P. Mohan, and B.-Q. Lao, "Radio frequency interference mitigation," *arXiv preprint arXiv:1711.01978*, 2017.
- [24] S. Joardar and A. Bhattacharya, "Design and analysis of a low-frequency radio telescope for jovian radio emission," *Progress In Electromagnetics Research*, vol. 72, pp. 127–143, 2007.
- [25] L. J. Lanzerotti, "Space weather effects on communications: An overview of historical and contemporary impacts of solar and geospace disturbances on communications systems," *Space storms and space weather hazards*, pp. 313–334, 2001.
- [26] A. Penzias and C. Burrus, "Millimeter-wavelength radio-astronomy techniques," *Annual Review of Astronomy and Astrophysics*, vol. 11, no. 1, pp. 51–72, 1973.
- [27] A. Leshem and A.-J. Van der Veen, "Radio-astronomical imaging in the presence of strong radio interference," *IEEE Transactions on Information Theory*, vol. 46, no. 5, pp. 1730–1747, 2000.
- [28] N. R. Council, D. on Engineering, P. Sciences, B. on Physics, C. on Radio Frequencies, and C. on Scientific Use of the Radio Spectrum, *Spectrum management for science in the 21st century*. National Academies Press, 2010.
- [29] B. Bean, S. Bhatnagar, S. Castro, J. D. Meyer, B. Emonts, E. Garcia, R. Garwood, K. Golap, J. G. Villalba, P. Harris *et al.*, "Casa, the common astronomy software applications for radio astronomy," *Publications of the Astronomical Society of the Pacific*, vol. 134, no. 1041, p. 114501, 2022.
- [30] A. J. Emrich and N. D. Whyborn, "Suggestions for some single dish radio astronomy standards," *Experimental astronomy*, vol. 4, pp. 41–58, 1993.
- [31] Y. Dai and H. Minn, "A spectrum sharing paradigm for gso satellite system and radio astronomy system," *IEEE Access*, vol. 7, pp. 93952–93973, 2019.
- [32] C. A. Balanis, *Antenna theory: analysis and design*. John wiley & sons, 2016.
- [33] S. Rudenko, D. Dettmering, J. Zeithöfler, R. Alkhal, D. Upadhyay, and M. Bloßfeld, "Radial orbit errors of contemporary altimetry satellite orbits," *Surveys in Geophysics*, vol. 44, no. 3, pp. 705–737, 2023.
- [34] D. A. Roshi, W. Shillue, B. Simon *et al.*, "Performance of a highly sensitive, 19-element, dual-polarization, cryogenic l-band phased-array feed on the green bank telescope," *The Astronomical Journal*, vol. 155, no. 5, p. 202, 2018.

- [35] L. A. Bronckers, A. Roc'h, and A. B. Smolders, "Benchmarking a high-end smartphone's antenna efficiencies," *IEEE Access*, vol. 7, pp. 105 680–105 686, 2019.
- [36] Z. Ying, "Antennas in cellular phones for mobile communications," *Proceedings of the IEEE*, vol. 100, no. 7, pp. 2286–2296, 2012.
- [37] B. Peterson, D. Bruckner, and S. Heye, "Measuring gps signals indoors," in *Proceedings of the 10th International Technical Meeting of the Satellite Division of The Institute of Navigation (ION GPS 1997)*, 1997, pp. 615–624.
- [38] D. Micheli, A. Delfini, M. Marchetti, P. Gianola, G. Bertin, and R. Diana, "Measurements of the outdoor-to-indoor attenuation of mobile phone signal," *International Journal on Communications Antenna and Propagation (IRECAP)*, vol. 4, no. 6, 2014.
- [39] V. Bui, N. T. Le, T. L. Vu, V. H. Nguyen, and Y. M. Jang, "Gps-based indoor/outdoor detection scheme using machine learning techniques," *Applied Sciences*, vol. 10, no. 2, p. 500, 2020.
- [40] "<https://www.skyworksinc.com/product-specification?family=amplifier&scategories=low>